PAPER

Metallo-deuteroporphyrins derived multi-layered hollow carbon spheres electrocatalysts for highly efficient oxygen reduction reaction

IOP Publishing Nanotechnology
Nanotechnology 32 (2021) 235401 (10pp) https://doi.org/10.1088/1361-6528/abeb9d

Metallo-deuteroporphyrins derived multi-layered hollow carbon spheres electrocatalysts for highly efficient oxygen reduction reaction

Han Zhang[1], Yue Wang[1], Shaojun Liu[1], Chenglong Li[1], Lixiang Li[1], Baigang An[1] and Chengguo Sun[1,2]

[1] School of Chemical Engineering, University of Science and Technology Liaoning, Anshan 114051, People's Republic of China
[2] School of Chemical Engineering, Nanjing University of Science and Technology, Nanjing 210094, People's Republic of China

E-mail: sunyangguo2004@163.com

Received 20 December 2020, revised 24 February 2021
Accepted for publication 3 March 2021
Published 19 March 2021

Abstract

The development of low-cost, highly efficient and stable non-precious metal electrocatalyst for the oxygen reduction reaction (ORR) substituting Pt has attracted much attention. Herein, we developed a promising structural platform for the fabrication of carbon nanospheres functionalized with hollow nanostructures of M-NHCS (M = Fe, Co and Mn) based on metallo-deuteroporphyrins (MDP). Benefited from the multi-layered active sites and hollow substrate with more exposed active surface area, convenient channels for the transport of electrons, the resulting Fe-NHCS electrocatalysts exhibit enhanced electrocatalytic performance in ORR with an onset potential of 0.90 V (versus RHE), and a high selectivity in the direct 4-electron pathway. The Fe-NHCS electrocatalysts also show a good methanol tolerance superior to Pt/C catalysts and an extremely high stability with only 13.0 mV negative after 5000 cycles in alkaline media. Experiments have verified that maintaining the multi-layered Fe−N−C active sites and hollow substrate were essential to deliver the high performance for ORR. The work opens new avenues for utilizing MDP-based materials in future energy conversion applications.

Supplementary material for this article is available online

Keywords: hollow carbon nanospheres, oxygen reduction reaction, non-precious metal catalysts, electrocatalysis, metallo-deuteroporphyrins

(Some figures may appear in colour only in the online journal)

1. Introduction

With the increasing consumption of traditional energy, energy shortage becomes a very serious problem in the world, and the environmental pollution caused by the excessive use of the nonrenewable energy resources also threatens the survival and development of human beings, such as heavy smog, global warming [1]. Developing the renewable, green and clean energy is much desired [2–4]. At present, the most promising alternatives for the capacity to efficient convert and store renewable power sources are fuel cells [5] and metal-air batteries [6–8]. Among them, polymer electrolyte membrane fuel cells (PEMFCs) are considered to be of great importance as the most advanced representative of fuel cell technologies to provide cleaner energy conversion [9]. It has the advantages of easy operation, high specific power, low operating temperature, fast start-up and long lifespan [10–12]. However, the oxygen reduction reaction (ORR), occurring at the

cathode of PEMFCs, exhibits the sluggish reaction kinetics, which affects energy-conversion efficiency and blocks the large-scale commercial applications of PEMFCs [10, 13, 14]. Platinum and its alloys are generally used as the effective catalysts for ORR [15, 16], however, their suffers from high cost, scarcity, poor methanol tolerance and low stability, which has been the bottlenecks that hamper widespread commercialization of PEMFCs [17–19]. Therefore, it is highly challenging and desirable to prepare alternative the low-cost catalysts with long-term stability and high electrocatalytic performance for ORR [20].

During the past decades, the intensive studies have demonstrated that earth-abundant and efficient non-precious metal catalysts have become promising alternatives to Pt-based catalysts, including transition-metal [21], metal oxide [22, 23], metal nitrogen-doped carbon [24, 25] and metal-free doped carbonaceous materials [26, 27]. Among the above non-precious metal materials, the transition metal−nitrogen −carbon (M−N−C) catalysts have been regarded as the most promising substitute due to their high ORR activity and low-cost [28–30]. Notably, macrocycles molecule, such as porphyrins, phthalocyanines contained abundant the metal (Fe or Co)–N_4 sites [31, 32]. The M−N_4 structure is considered to be the active site of ORR catalysts, it can be traced back to the United States scientist Jasinski who discovered the cobalt phthalocyanine molecule was mixed with Ni powder showed excellent ORR activity [33]. However, the ability of macrocyclic structure against oxidative degradation is weak, resulting in the deteriorated stability of catalysts. The current solutions are used the high-temperature pyrolysis process of macrocyclic metal-phthalocyanines or porphyrins precursor to generate highly active metal-N_x sites to improve their stability. Lu and co-workers reported the development of a cobalt (II) porphyrin based porous organic polymer (CoPOP) and its pyrolyzed derivatives as highly active ORR catalysts [34]. The as-synthesized CoPOP exhibits high porosity and excellent catalytic performance stability. Although the active species of metallic macrocycles are controversial, it is generally accepted that pyrolysis of the complexes enhance the ORR activity. The amount of N and metal species of carbon materials are essential to activities. with the help of N coordination, the activity of metal species for ORR were enhanced obviously [35]. Besides, the active sites of M−N_4 have great influence on ORR, but it is still great challenge to design efficient metal nitrogen-doped carbon catalysts for PEMFC [36].

Metallo-deuteroporphyrins (MDP) have been attracted great attention due to the unique properties, wide derivatives and relatively cheap cost, which also can act as an electrochemical sensor to detect hydrogen peroxide and oxygen in the solution [37]. Pyrolyzed MDP as non-platinum catalyst for PEMFC cathode catalyst application has few reported so far. Therefore, it is necessary to deepen the research and enrich the relevant basic and theoretical knowledge [38].

Herein, we applied a hard template method to construct the high activity and stable multi-layered hollow carbon sphere electrocatalysts (M-NHCS-X, M = Fe, Co and Mn, X = 600 °C, 700 °C, 800 °C and 900 °C). The amino-functionalized silicon spheres were used as templates, and MDP were used to as both carbon precursor and metal active center. It is worth mentioning that MDP were chosen as precursor because of well-defined structure, and versatile functions, which can be grafted on the surface of amino-functionalization of SiO_2 nanospheres and then coated by polypyrrole (PPy). After a facile carbonization process and acid treatment to etch away SiO_2 template, the electrocatalysts were obtained. The multi-layered hollow carbon sphere catalysts exhibit a favorable cathode catalyst in PEMFC applications as it contributes to excellent activity, superior methanol-tolerant and stability for ORR.

2. Experiment

A series of MDP was prepared according to the method described in the literature [39]. 3-aminopropyltriethoxysilane was supplied by Nanjing YouPu chemical Reagents (China). Hydrofluoric acid (HF, 40%) was purchased from shanghai Macklin chemical Reagents (China). 5 wt% Nafion (DuPont, US) and JM 20% Platinum carbon were purchased form Kunshan pterson international trade chemical Reagents. The distilled water was generated with a Mill-Q integral pure and ultrapure water purification system. Other reagents, such as ammonia, tetraethyl orthosilicate, anhydrous ethanol, dichloromethane, triethylamine, toluene, sulfoxide chloride, pyrrole, potassium hydroxideand Iron (III) chloride hexahydrate were obtained from Sinopharm Chemical Reagent Co., Ltd (Shanghai, China). All the chemicals used in this experiment were analytical grade used without further purification.

2.1. Synthesis of SiO_2 nanospheres

Inspired by the classic StÖber method, we prepared the different sized silica spheres by our improved synthesis method. Taking the synthesis of ∼320 nm silica spheres as an example, 70 ml of absolute ethanol and TEOS (6 ml) were mixed in beaker, 25 ml of distilled water and 2 ml of $NH_3{\cdot}H_2O$ (28%) were added into the mixture with kept stirring at 600 rpm for 2 h at room temperature. The obtained product was separated by centrifugation, washed subsequently with the mixture of ethanol and distilled water for third times, and finally dried up.

2.2. Synthesis of amino-functionalization of SiO_2 nanospheres

SiO_2 (4 g) was dispersed in 150 ml of toluene. The mixture was sonicated for 30 min, subsequently injected into 4 ml of 3-aminopropyltriethoxysilane. The mixed solution was then transferred into round bottle flask with refluxed and stirred at 110 °C for 5 h under nitrogen atmosphere. After cooling to room temperature, the suspension was then filtered and the solid residues were washed thoroughly with CH_2Cl_2 for twice and finally dried at 80 °C under vacuum for 6 h to obtain milky solid of SiO_2–NH_2.

2.3. Synthesis of core−shell SiO_2–NH_2–MDP (M = Fe, Co and Mn) nanospheres

MDP (0.6 g) was dispersed in 50 ml of CH_2Cl_2 under sonication, where was added dropwise sulfoxide chloride (0.4 ml). The mixed solution was then magnetically stirred at 110 °C for 4 h under nitrogen atmosphere. The solvent was vacuumed and removed CH_2Cl_2 at 70 °C until the bottom of the round bottle flask formed a black lump, followed by added into 20 ml of CH_2Cl_2 under ultrasound to form solution. The suspension subsequently vacuumed and removed CH_2Cl_2 at 60 °C. Then SiO_2–NH_2 (0.5 g), 30 ml of dichloromethane and 2.5 ml of triethylamine were added to the above solution in turn. The mixture was refluxed and stirred at 40 °C for 3 h. The suspension was then filtered and the solid residues was washed thoroughly anhydrous ethanol for several times, finally dried at 80 °C under vacuum for overnight to obtain black brown solid of SiO_2-NH_2-MDP (M = Fe, Co and Mn). The SiO_2-MDP was prepared with SiO_2 under identical conditions for comparison.

2.4. Synthesis of pyrrole encapsulated on SiO_2-NH_2-MDP nanospheres

0.3 g of SiO_2-NH_2-MDP was added to a mixture solution of ethanol (50 ml) and distilled water (20 ml) under sonicated for 1 h. Then 0.3 ml of pyrrole was added and stirred for 30 min The solution of 0.9 g $FeCl_3{\cdot}6H_2O$ dissolved in 30 ml of water was added dropwise the above mixed solution. The derived mixture vigorous stirring at 21 °C for 15 h. Finally, the sample was successively washed several times with water during filtration. The black solid was noted as SiO_2-NH_2-MDP-ppy.

2.5. Synthesis of M-NHCS-X (X = 600 °C, 700 °C, 800 °C, 900 °C), NHCS@Fe-700, Fe-HCS-700 and HCS-700

The Fe-NHCS-X and NHCS@Fe-700 were prepared by thermal treatment of SiO_2-NH_2-Femin-ppy and SiO_2-Femin-ppy with a ramp rate of 5 °C min^{-1} at a temperature ranging from 600 °C to 900 °C for 2 h in the protection of argon gas (denoted as Fe-NHCS-600, Fe-NHCS-700, Fe-NHCS-800 and Fe-NHCS-900). After the carbonization, the template of SiO_2 template was removed by hydrofluoric acid (40 wt%) at room temperature for 24 h and collected by centrifugation, washed subsequently with water and ethanol for third and finally dried at 80 °C under vacuum for overnight. The corresponding Co-NHCS-X and Mn-NHCS-X were prepared by the same procedure as for Fe-NHCS. The Fe-HCS-700 and NCS-700 were prepared without pyrrole and MDP, respectively, under identical conditions for comparison.

2.6. Material characterization

The morphology, composition and structure of catalysts were characterized by scanning electron microscopy (SEM) (ΣIGMA/HD), transmission electron microscopy (TEM) (JEOLJEM-2100), XRD (D/Max2500 with Cu Ka x-ray source), Raman (HORIBA Xplora Plus), Brunauer−Emmett−Teller (BET) (ASAP-2020). FT-IR (EQUINOX55), XPS (the chemical states of N, C, Fe, and Co elements. All the collected binding energies were calibrated by using the C1s peak at 284.6 eV as the reference with an uncertainty of ± 0.2 eV).

2.7. Electrochemical measurement

All the electrochemical measurements were carried out at room temperature with a Gamry Reference 3000 potentiostat was employed, together with a Gamry's Rotating Disk Electrode (RDE710) equipped with a conventional three-electrode system. Ag/AgCl electrode (saturated with KCl, 0.1989 V versus RHE) and graphite rod (Gamry, USA) were used as reference and counter electrode, respectively. A RDE with a glassy carbon (GC) disk with a diameter 5 mm (surface area = 0.196 25 cm^2) was used as the working electrode. The preparation of a working electrode is as follows: 8.0 mg of the as-prepared samples was dispersed in 1.0 ml of ethanol with 50 μl of 5 wt% Nafion solution by sonication to obtain a homogeneous black suspension solution for 1 h, the 10 μl of ink was pipetted onto the GC disk electrode surface and allowed to dry with infrared lamp for 5 min, resulting in catalyst loading of 0.4 mg cm^{-2}. For comparison, Pt/C was used as the baseline catalyst under the same measuring conditions. The electrolyte was bubbled with O_2 for about 30 min to achieve the O_2-saturated solution before each test. The cyclic voltammetry (CV) experiments were cycled in 0.1 M KOH solution under O_2 or N_2–saturation conditions with a scan rate of 50 mV s^{-1}. The RDE measurements were performed at various rotating speed from 400 to 2500 rpm in 0.1 M KOH solution under O_2–saturation conditions with a scan rate of 10 mV s^{-1} at room temperate. During the measurement, oxygen was only passed over the surface of the electrolyte. Moreover, the accelerate durability tests (ADT) was used to evaluate the stability of M-NHCS-X (M = Fe, Co and Mn) under continuous O_2-bubblings 0.1 M KOH solution using potential cycling between 0.87 V and 1.17 V with the sweep rate of 100 mV s^{-1} at room temperature.

3. Results and discussion

3.1. Synthesis and characterization

The preparation strategy of the M-NHCS-X (M = Fe, Co, and Mn, X = 600 °C, 700 °C, 800 °C and 900 °C) is briefly illustrated in Scheme 1. Typically, the preparation involves three steps. Firstly, the grafting of MDP onto the surface of amino-functionalized SiO_2 nanospheres by amidation reaction. Then, PPy nano-coating is carried out by the controlled polymerization of pyrrole around the SiO_2-NH_2-MDP nanospheres in the presence of $FeCl_3{\cdot}6H_2O$ at room temperature. Finally, as-obtained SiO_2-NH_2-MDP nanospheres was converted to M-NHCS-X by thermal annealing at temperature ranging from 600 °C to 900 °C under Ar

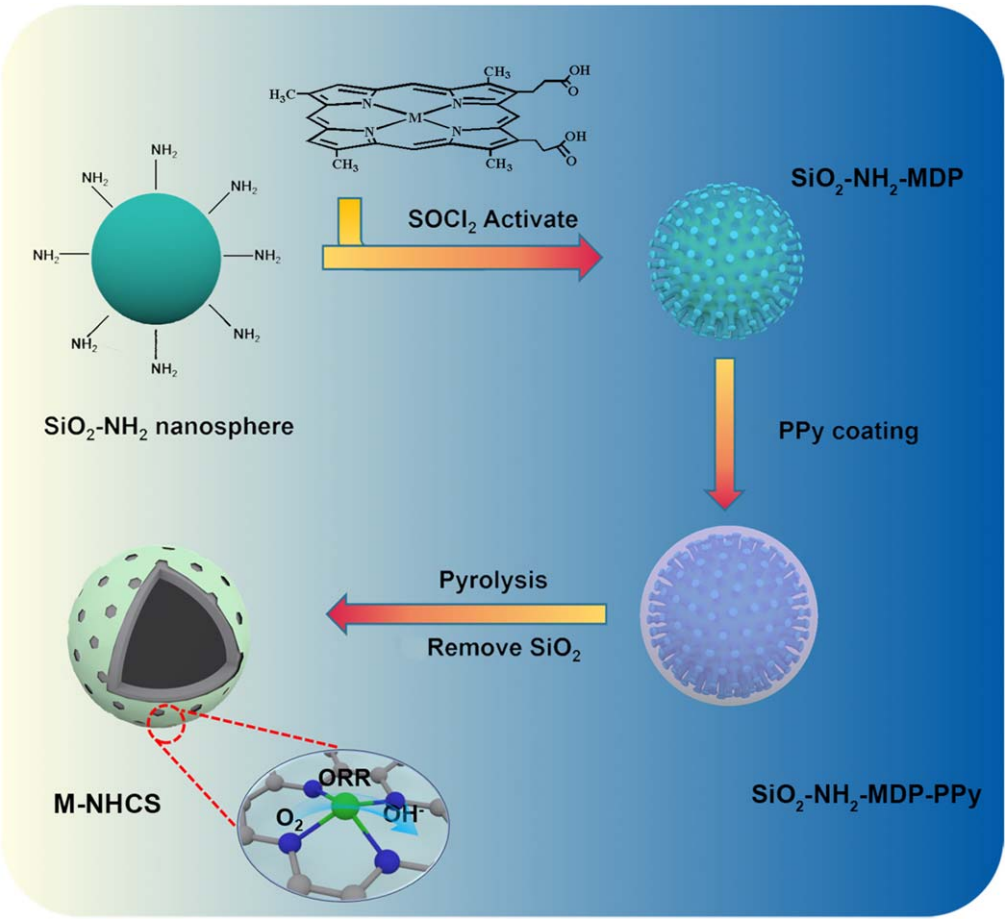

Scheme 1. Schematic illustration of preparation procedures for the M-NHCS (M = Fe, Co and Mn).

atmosphere, followed by HF etching to remove SiO_2 template.

The morphology and microstructure of the as-synthesized materials were determined by SEM and TEM. SEM images of SiO_2 nanospheres and M-NHCS-X (M = Fe, Co and Mn) catalysts are shown in figures 1 and S1–2 (available online at stacks.iop.org/NANO/32/235401/mmedia). The highly uniform SiO_2 nanospheres with a smooth spherical morphology and a diameter of ~340 nm could be obtained by the StÖber method. The SiO_2 spheres are intact, discrete, and monodisperse. After coating and carbonization, the surface of as-prepared particles became much rougher and kept the SiO_2 spheres shape (figures 1(b), S1 and S2). The outer diameter and the wall thickness of as-prepared particles are estimated to be ~340 nm and 20 nm, respectively (figure 1(d)), in agreement with the size of SiO_2 templates. The uniform hollow structures are confirmed by a few broken nanospheres with clearly exposed internal cavities (figure 1(c)) and TEM (figure 1(d)). The high-angle annular dark field-scanning transmission electron microscope (HAADF-STEM) image and mapping analysis of Fe-NHCS-700 (figure 1(e)) reveal that C, N, Fe and O are homogeneously distributed along the catalyst, which could also be observed from the results obtained by the full spectrum of XPS (figure S7).

X-ray diffraction was performed to investigate the crystallographic phase of the as-prepared composites. The XRD

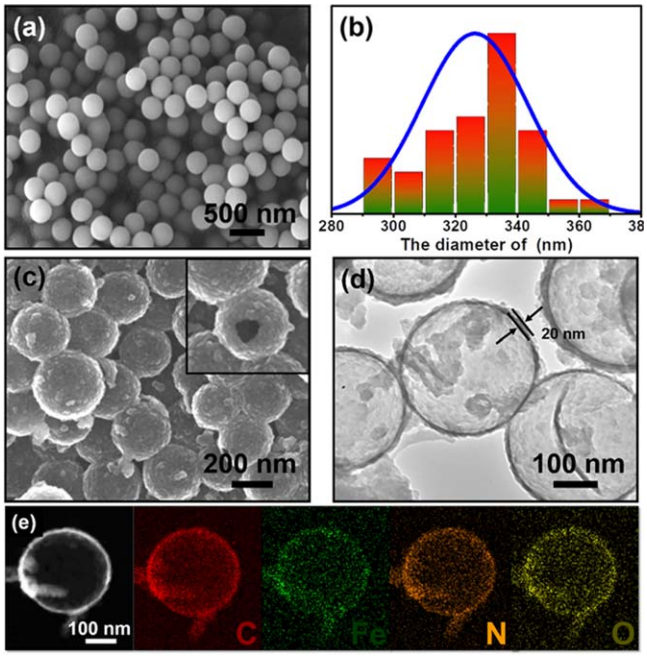

Figure 1. SEM images of (a) SiO_2 nanospheres and (c) Fe-NHCS-X. (b) the diameter distribution histogram of SiO_2 nanospheres (d) TEM image and (e) HAADF-STEM image of Fe-NHCS-700 and corresponding elemental mappings of C, Fe, N and O.

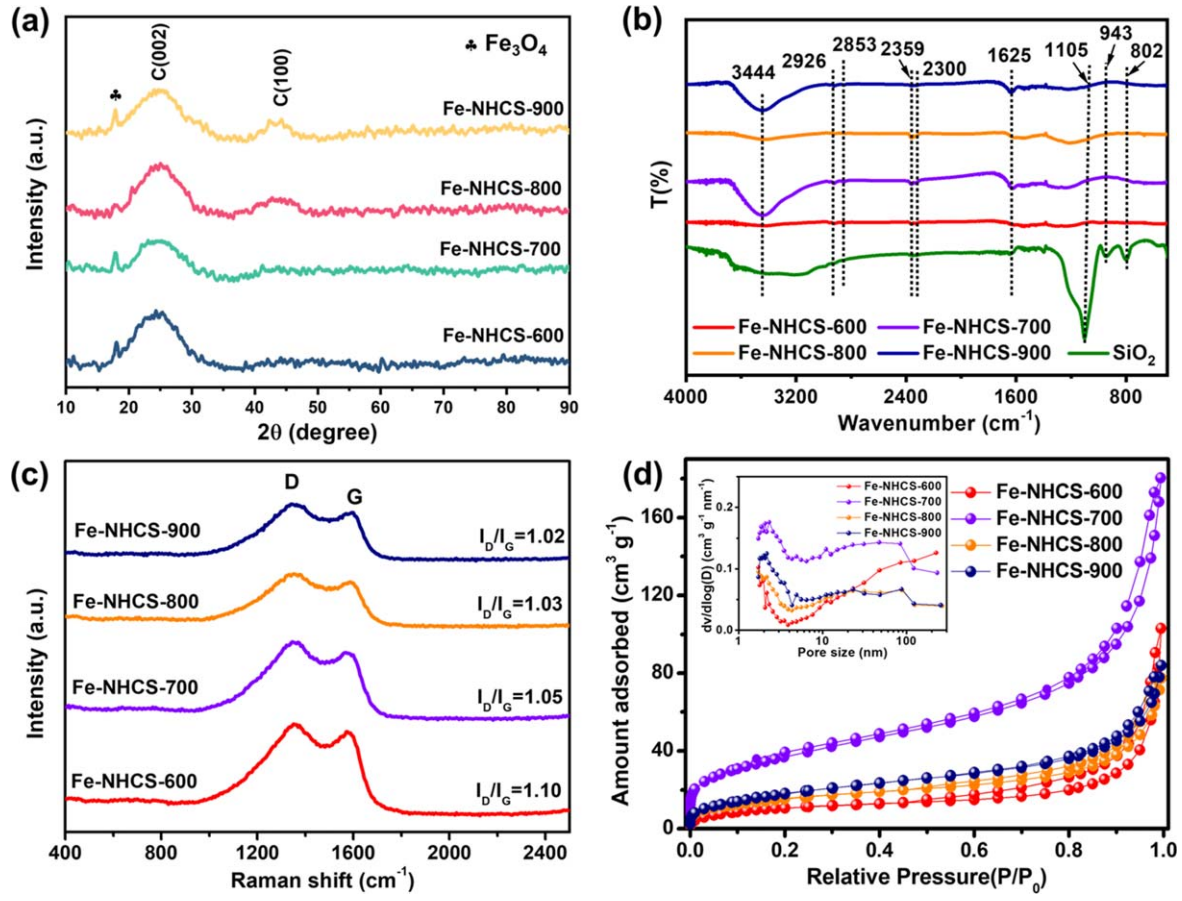

Figure 2. (a) XRD patterns of the Fe-NHCS-X. (b) FT-IR spectra of Fe-NHCS-X and SiO_2 nanospheres. (c) Raman spectra, (d) N_2 adsorption−desorption isotherm at 77 K and the corresponding pore size distribution (BJH method) of the Fe-NHCS-X.

patterns of M-NHCS-X are presented in figure 2(a) and S3. Obviously, Fe-NHCS-X show a broad diffraction peak and weak peaks at around 26.5° and 43°, corresponding to the (002) and (100) plane of the graphite structure (PDF#41-1487) [40], respectively, while the well-defined peak at around $2\theta = 18.3°$ match well with Fe_3O_4 (PDF#75-0033), implying the presence of graphitic carbon and Fe_3O_4 in Fe-NHCS-X [41]. The functional groups present in the M-NHCS-X electrocatalyst were characterized using Fourier transform infrared spectrometer (FT-IR). Figure 2(b) shows that the FT-IR spectrum of Fe-NHCS-X electrocatalysts. In contrast, the FT-IR of SiO_2 nanospheres were given for index. The wider peak at around 3444 cm^{-1} corresponds to the N−H stretching vibration and the peak at around 2900–2800 cm^{-1} is saturated C−H stretching vibration. The absorption peak at around 2300–2360 cm^{-1} corresponds to C−O stretching vibration. FT-IR showed a strong band at 1105 cm^{-1}, which is antisymmetric stretching vibration peak of Si−O−Si, as well as the peak at around 943 and 802 cm^{-1}, which can be assigned to symmetrical telescopic vibration peak and the bending vibration peak of Si−O−Si, respectively. The without SiO_2 template of M-NHCS-X has almost the same infrared spectrum (figure 2(b) and S4), indicating successful replication of the template, and SiO_2 sphere used in the experiment has been basically eliminated after acid etching.

Raman spectroscopy is widely used to investigate the graphitic structures, defects and disordered phases of as-prepared catalyst hybrids. Figure 2(c) shows the Raman spectra of Fe-NHCS-X flakes, and displays two characteristic peaks at 1329, 1590 cm^{-1}, which were assigned to the D and G bands, respectively. The D band corresponds to sp^3 defects and disordered sites, the G band refers to the sp^2-hybridized graphitic structure and usually corresponds to the degree of graphitization [42]. The relative intensity ratio of the G band and D band peaks (I_D/I_G) is used to estimate the amount of defects and disordered structures in the carbon structure. The small I_D/I_G value suggests the presence of more ordered graphitic carbon, which improves the electrical conductivity and is beneficial for the electron transfer during ORR. The I_D/I_G values of Fe-NHCS-X (X from 600 °C to 900 °C) are 1.10, 1.05, 1.03 and 1.02, respectively (figure 2(b)), as well as the I_D/I_G values of Co-NHCS-X are 1.15, 1.12, 1.10 and 1.05 (Figure S5), respectively, implying that a higher pyrolysis temperature promotes the formation of an ordered graphitic structure of the carbon. Notably, compared with Co-NHCS-700 (1.12), the I_D/I_G value observed for Fe-NHCS-700 was 1.05, demonstrating the higher graphitization degree of Fe-NHCS-700, and carbon graphitization in the catalysts can enhance the electronic conductivity and corrosion resistance in electrocatalysis [43, 44]. M-NHCS-X were evaluated by measuring the N_2 adsorption−desorption isotherm techniques

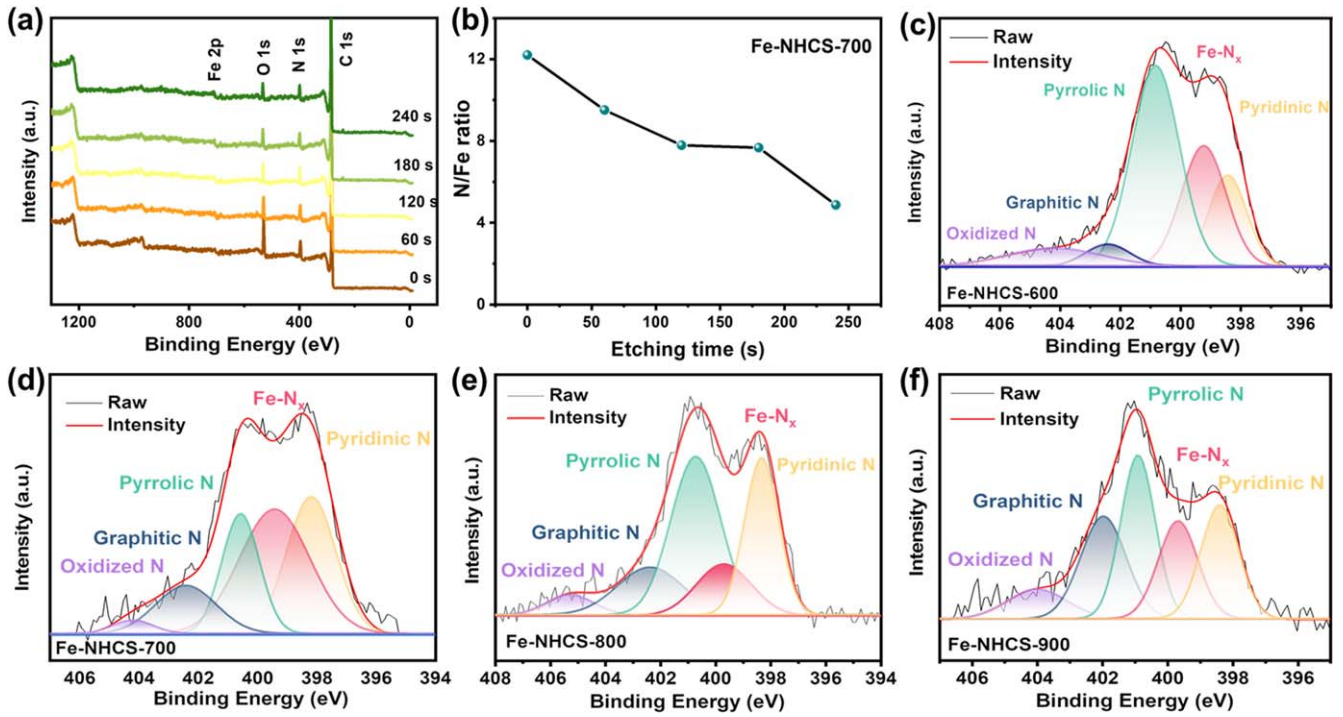

Figure 3. (a) Depth XPS full spectra and (b) N/Fe ratio for Fe-NHCS-700 at different Ar etching time of 0, 60, 120, 180 and 240 s. High-resolution N 1s of the (c) Fe-NHCS-600, (d) Fe-NHCS-700, (e) Fe-NHCS-800 and (f) Fe-NHCS-900.

at 77 K to explore the change of pore structure and surface area. According to the curves of M-NHCS-X, the type IV isotherm and H4-type hysteresis loops following the IUPAC classification can be observed in figures 2(d), S6(a) and S6(c), suggesting the existence of mesopores for M-NHCS-X samples [45]. The BET surface area of hollow Fe-NHCS-700 spheres is 133.4 m^2 g^{-1} after etching, which is significantly larger than that of other samples, while the specific data for all samples were summarized in table S1. However, the nitrogen isotherm of Fe-NHCS-700 exhibits a significant rise at a high relative pressure, suggesting the porous structure derived from the hollow interior. The Barrett−Joyner−Halenda (BJH) pore size distribution curves (figures 2(d), S6(b) and S6(d)), further confirms the presence of porous structure in the obtained HNSs with a pore size centered at 7.9 nm for Fe-NHCS-700, 5.1 nm for Co-NHCS-700, and 15.1 nm for Mn-NHCS-700, respectively (table S1). It is mentionable that porous architecture with a large specific surface area of the Fe-NHCS-700 is beneficial for facilitating the exposure of more active sites and the electron/ion transportation efficiently, thus improving electrochemical activities of the composites.

The Fe-NHCS-700 were further analyzed by depth XPS with different etching times of Ar ion treatment to investigate the difference of chemical composition and surface electronic state (figures 3(a)–(b) and S7). As etching time increases, the N/Fe ratio of content for the Fe-NHCS-700 decreases (12.2 at 0 s and 4.87 at 240 s, etc), which is indicting multi-layered structure from surface to interior. As shown in figure S8(a), the XPS full survey of Fe-NHCS-X exhibits several sharp peaks, indicating the presence of C, N, and O in the obtained composites. Figure S8(b) shows the high-resolution Fe 2p spectrum. The peaks at 710.8 and 713.7 eV can be assigned to the binding energies of the $2p_{3/2}$ orbitals of Fe^{2+} and Fe^{3+} species, respectively. For the $2p_{1/2}$ band, the peak at 725.2 eV is attributed to the binding energy of Fe^{2+}, and the peak for Fe^{3+} is observed at 726.4 eV. The satellite Fe $2p_{3/2}$ peak at 718.6 eV also indicated the existence of iron oxide phase in the carbon material [25]. And no peak between 700.0 and 708.0 eV is assigned to zero-valence iron, indicating that the iron atom is mostly coordinated with the surrounding nitrogen atoms [46, 47].

As shown in figures 3(c)–(f), the high-resolution spectra of N 1s region can be fitted with three peaks at 398.4, 399.2, 400.8, 402.4 and 404.2 eV assigned to the coexistence of pyridinic, Fe−N_x, pyrrolic, and graphitic nitrogen species and oxidized N, respectively, suggesting that N is doped into the carbon molecular skeleton [48, 49]. The previous studies suggested that the nitrogen-doped carbon materials show excellent charge mobility in the carbon atom matrix, which can accelerate the catalytic activity in electron-transfer reactions. In contrast, the Fe-NHCS-700 sample has the relative largest content of pyridinic N and Fe−N_x content, which can be responsible for the electrocatalytic activity in ORR [50–52].

3.2. Electrochemical evaluation

To assess the electrocatalyst activities of Fe-NHCS-X, Co-NHCS-X and Mn-NHCS-X for ORR, as-synthesized electrocatalyst was tested in O_2-saturated 0.1 M KOH electrolyte were recorded at a scan rate of 50 mV s^{-1}. Figure 4(a) and figure S9 shows the CV measurements of Fe-NHCS-X. The significant reduction peak was observed at 0.78 V in the

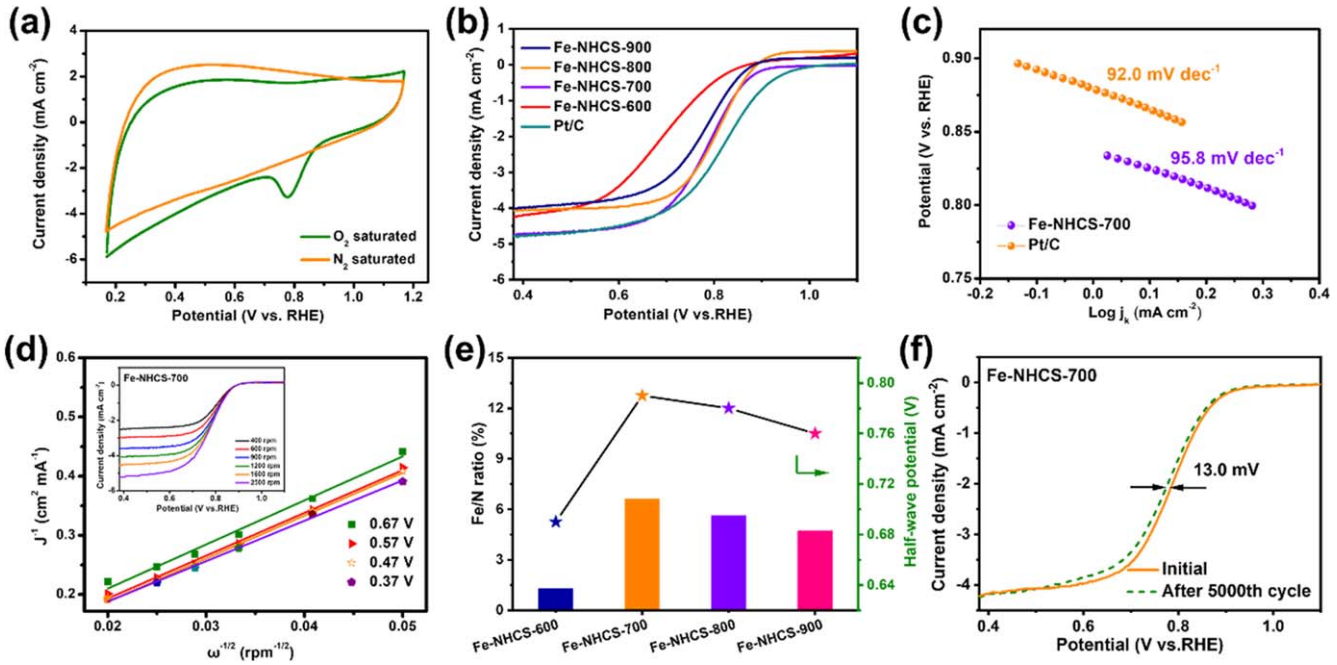

Figure 4. (a) CV curves of Fe-NHCS-700 catalysts in KOH solution saturated by N_2 or O_2 at a scan rate of 50 mV s^{-1}. (b) ORR polarization curves of Fe-NHCS-X (X = 600, 700, 800 and 900) and commercial Pt/C electrodes and (c) Tafel plots of Fe-NHCS-700 and Pt/C at a rotation rate of 1600 rpm at a scan rate of 10 mV s^{-1}. (d) K–L plots of the Fe-NHCS-700 derived from data in the inset under different potentials. (e) The Fe/N ratio of the as-prepared Fe-NHCS-X with respect to the ORR activity. (f) LSV curves of the Fe-NHCS-700 catalysts for ORR in O_2-staurated 0.1 M KOH before and after 5000 cycles.

O_2-saturated solution, while within the same voltage window, only featureless quasi-rectangular voltammogram is observed in N_2-saturated electrolyte. To further examine the ORR activity of Fe-NHCS-X, Co-NHCS-X, and Mn-NHCS-X were investigated by using RDE experiments at 1600 rpm in O_2-saturated 0.1 M KOH solution (figure 5(d)). Pt/C catalyst was used for comparison (figure 4(b)). The results suggest that the Fe-NHCS-700 electrocatalyst has the high onset ORR potential (E_{onset}) of 0.90 V and half-wave potential ($E_{1/2}$) of 0.79 V, which is superior to the other three materials catalysts (Fe-NHCS-600, 800 and 900), Co-NHCS-X catalysts and Mn-NHCS-X catalysts (figures S11(a)–(d)), and approaches to the Pt/C tested under similar conditions ($E_{onset} = 0.94$, $E_{1/2} = 0.83$ V), and outperform most previously reported ORR catalysts (table S3). The corresponding calculated kinetic limiting current densities at (J_k) at 0.47 V of Fe-NHCS-X is 1.90, 3.90 3.43, and 2.10 mA cm^{-2} (figure S10), respectively. These results further verify that the Fe-NHCS-700 catalyst displays faster ORR electrocatalytic reaction kinetics than the Co-NHCS-X and Mn-NHCs-X catalysts. According to the LSV curves, the calculated Tafel slope of Fe-NHCS-700 catalyst (95.8 mV dec^{-1}) was close to Pt/C (92.0 mV dec^{-1}), suggesting the superior ORR kinetics of Fe-NHCS-700 and the advantage of hollow sphere structures for electrocatalytic activity (figure 4(c)).

To assess the electron-transfer mechanism, LSV were measured at a rate of 10 mV s^{-1} under rotation speeds of 400, 600, 900, 1200, 1600, and 2500 rpm. Then, the Koutecky–Levich (K–L) equation was used to calculate the electron-transfer number (figure 4(d)). The fitted lines suggested that the n value of Fe-NHCS-700 is 3.90, which is close to Pt/C (3.93) at 0.47 V, indicating the desired 4-electron oxygen reduction process and the reduction of O_2 to OH^-, as well as the similar electron-transfer numbers at different potentials. In contrast, the electron-transfer numbers of Co-NHCS-X in the wide range was nearly 2, indicating the Co-NHCS-X is 2-electron reduction pathway (figures S11(b), (c)), and the electron-transfer numbers of Mn-NHCS-X in the wide range was nearly 3, indicating the Mn-NHCS-X involves a mixed 2-electron/4-electron transfer pathway for ORR (figures S11 (e), (f)). Furthermore, the Fe/N ratio associated with the ORR activity was also investigated in figure 4(e), and the Fe-NHCS-700 (6.6%) with the highest Fe/N ratio showed a better ORR activity than that of the Fe-NHCS-600 (1.3%), and Fe-NHCS-800 (5.6%) and Fe-NHCS-900 (4.7%) catalysts. The more real active sites of Fe−N_x and pyridine N in the Fe-NHCS-700 catalyst were considered to be the active sites for enhancing the ORR activity [53].

Additionally, the methanol tolerance is also a significant index for the cathode materials of practical application in PEMFC. The Pt/C catalyst generally displays imperfect performances (figure S12). However, the Fe-NHCS-700 is resistant to methanol poisoning, exhibiting negligible decrease in current density, except for a slight oscillation. The Fe-NHCS-700 against methanol influence can be attribute to the doped N atoms and multi-layered active sites that can improve the electronic density, and enables the NHCSs to be electronically more negative, facilitating the reduction of O_2 rather than oxidation of methanol. An ADT was assessed by cycling the catalyst between 0.87 V and 1.17 V versus RHE was used to evaluate the stability of Fe-NHCS-700, Co-NHCS-700 and Mn-NHCS-700 at scan speed of 100 mV s^{-1}

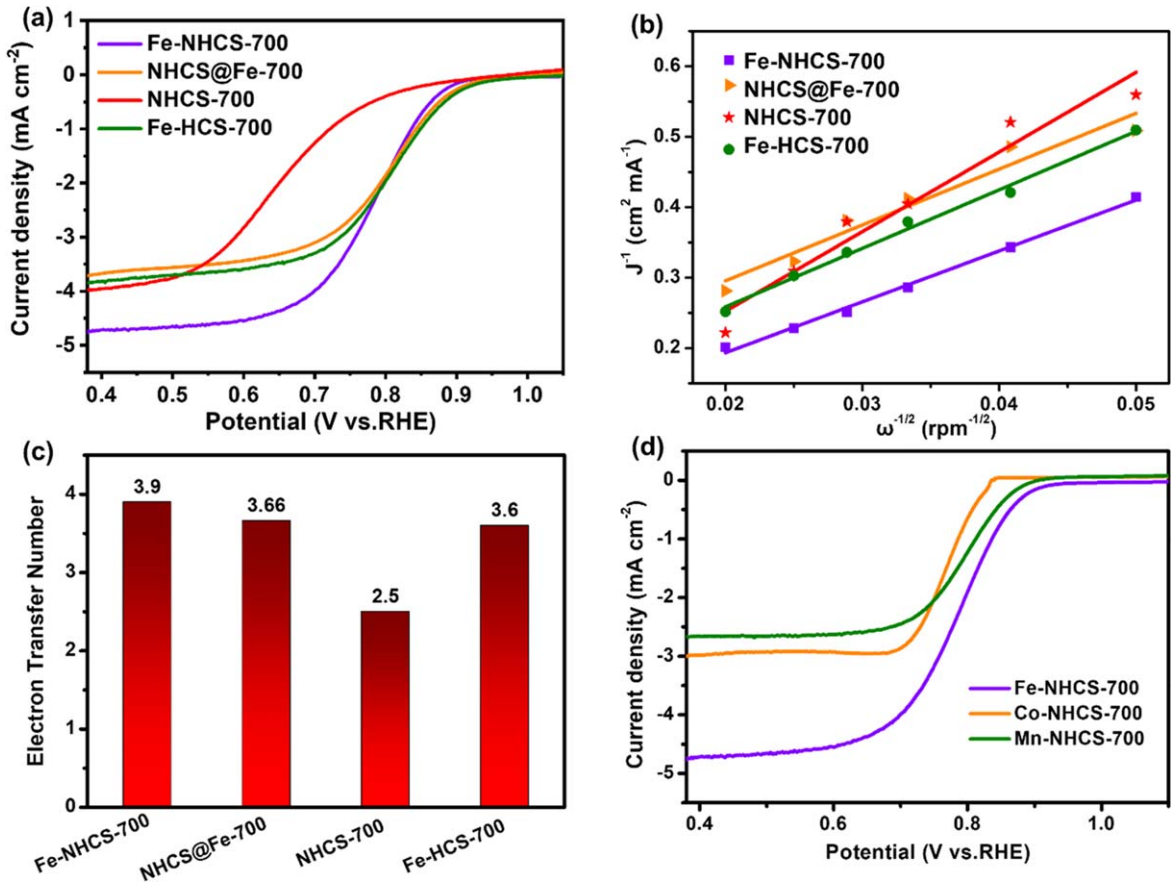

Figure 5. (a) RDE linear sweep voltammograms curves of Fe-NHCS-700, NHCS@Fe-700, NHCS-700 and Fe-HCS-700 electrodes in O_2-saturated 0.1 M KOH. Rotative rate: 1600 rpm. (b) K−L plots of the samples. (c) The number of electron transfer values. (d) ORR polarization curves of Fe-NHCS-700, Co-NHCS-700 and Mn-NHCS-700 electrodes at a rotation rate of 1600 rpm at a scan rate of 10 mV s^{-1}.

and then recording LSV sweeps at a scan rate of 10 mV s^{-1} with a rotational rate of 1600 rpm in O_2-saturated 0.1M KOH (figures 4(f) and S13). It can be seen that Fe-NHCS-700 exhibits a relatively smaller negative shift (13.0 mV versus 20 mV) in the $E_{1/2}$ value after 5000 cycle than Co-NHCS-700 (14.0 mV) and Mn-NHCS-700 (15.6 mV), revealing the better long-term stability of Fe-NHCS-700.

To assess the effects of different carbon coating for ORR, as-synthesized electrocatalysts were investigated by using RDE experiments at 1600 rpm in O_2-saturated 0.1 M KOH solution. As shown in figure 5(a), it can be seen that Fe-HCS-700, NHCS@Fe-700 and Fe-NHCS-700 have the same half-wave potential. Owing to the three samples have the carbonated MDP as the main active sites, making the activity stronger than that of hollow carbon spheres without MDP layer. The onset potential of Fe-NHCS-700 is higher than that of Fe-HCS-700, which indicates that the hollow carbon spheres coated by the outermost polypyrrole are more active than those exposed to the surface of MDP. The active species of MDP pyrolysis are easy to distribute on the surface of carbon layer, the strong acid or alkali conditions of the receptor system leads to the corrosion of outer carbon, which leads to the loss of active species formed by metal elements and nitrogen, thus reducing the oxygen reduction activity of the material. The Fe-NHCS-700 coated by polypyrrole carbonization can act as a protective clothing. In addition, the amount of nitrogen doping is increased, and the oxygen reduction activity is increased. The onset potential and half-wave potential of NHCS-700 are lower than those of the other three materials. Besides, the electron-transfer numbers of NHCS-700 can be regarded as the 2-electron pathway (figures 5(b)–(c) and S14), indicating that the activity of the main active sites of electrocatalyst without MDP intermediate layer is significantly lower than the samples with MDP as the main active sites [24]. It further verifies that the intermediate-layer MDP as the main active site is important role of materials in the sample. Compared to NHCS@Fe-700, Fe-NHCS-700 has higher onset potential and limiting current density, indicating the more rapid charge transfer attributed to the hollow nanostructure can expose very high fraction of surface sites. The multi-layered hollow carbon spheres electrocatalysts have large surface area and allow for increased collision frequency by confining reactants within nanoscale space.

4. Conclusion

In summary, we report a metallo-deuteroporphyrin-assisted strategy for synthesis of hollow carbon nanospheres decorated

with various metal nanoparticles. The Fe-NHCS-700 catalyst exhibited excellent catalytic activity for ORR with high tolerance towards methanol and great stability among the Fe-NHCS-X, Co-NHCS-X and Mn-NHCS-X catalysts studied. The onset potential of the Fe-NHCS-700 catalyst (0.90 V) was close to Pt/C (0.94 V) catalyst. The electron transfer number (n) involved in the ORR was calculated to be 3.90 at 0.47 V, illustrating a high selectivity in the direct $4e^-$ pathway and the full reduction of O_2 to OH^- through the direct $4e^-$ mechanism. The enhanced ORR properties were ascribed to the iron atoms coordinated N atoms, and hollow multilayered nanostructures that were essential to deliver the high performance with transporting electrons for ORR. The approach provided a promising structural platform for the fabrication of carbon nanospheres functionalized with hollow nanostructures of M−N−C.

Acknowledgments

The authors gratefully acknowledge the financial support provided by the National Natural Science Foundation of China (21701077, 11972178, 51672117, 51672118, 51872131 and 51972156), and the Talent Project of Revitalizing LiaoNing (XLYC1807114, 2019LNZD01, 2020LNQN17, 2019QN07).

Data availability statement

All data that support the findings of this study are included within the article (and any supplementary files).

Conflict of interest

The authors declare that they have no known competing financial interests or personal relationships that could have appeared to influence the work reported in this paper.

ORCID iDs

Chengguo Sun https://orcid.org/0000-0003-3580-2153

References

[1] Aristondo O and Onaindia E 2018 Counting energy poverty in Spain between 2004 and 2015 *Energy Policy* **113** 420–9
[2] Aized T, Shahid M, Bhatti A A, Saleem M and Anandarajah G 2018 Energy security and renewable energy policy analysis of Pakistan *Renew. Sustain. Energy Rev.* **84** 155–69
[3] Damette O, Delacote P and Lo G D 2018 Households energy consumption and transition toward cleaner energy sources *Energy Policy* **113** 751–64
[4] Li L, Wu Z, Yuan S and Zhang X-B 2014 Advances and challenges for flexible energy storage and conversion devices and systems *Energy Environ. Sci.* **7** 2101–22
[5] Wu G, More K L, Johnston C M and Zelenay P 2011 High-performance electrocatalysts for oxygen reduction derived from polyaniline, iron, and cobalt *Science* **332** 443–7
[6] Flegler A, Hartmann S, Settelein J, Mandel K and Sextl G 2017 Screen printed bifunctional gas diffusion electrodes for aqueous metal-air batteries: combining the best of the catalyst and binder world *Electrochim. Acta* **258** 495–503
[7] Li X, Liu Z, Song L, Wang D and Zhang Z 2018 Three-dimensional graphene network supported ultrathin CeO_2 nanoflakes for oxygen reduction reaction and rechargeable metal-air batteries *Electrochimi. Acta* **263** 561–9
[8] Xu N, Zhang Y, Zhang T, Liu Y and Qiao J 2019 Efficient quantum dots anchored nanocomposite for highly active ORR/OER electrocatalyst of advanced metal-air batteries *Nano Energy* **57** 176–85
[9] Wang Y-J, Long W, Wang L, Yuan R, Ignaszak A, Fang B and Wilkinson D P 2018 Unlocking the door to highly active ORR catalysts for PEMFC applications: polyhedron-engineered Pt-based nanocrystals *Energy Environ. Sci.* **11** 258–75
[10] Guo L, Jiang W-J, Zhang Y, Hu J-S, Wei Z-D and Wan L-J 2015 Embedding Pt nanocrystals in N-doped porous carbon/carbon nanotubes toward highly stable electrocatalysts for the oxygen reduction reaction *ACS Catal.* **5** 2903–9
[11] Lopez Lopez G, Schacht Rodriguez R, Alvarado V M, Gomez-Aguilar J F, Mota J E and Sandoval C 2017 Hybrid PEMFC-supercapacitor system: Modeling and energy management in energetic macroscopic representation *Appl. Energy* **205** 1478–94
[12] Pei H, Liu Z, Zhang H, Yu Y, Tu Z, Wan Z and Liu W 2013 In situ measurement of temperature distribution in proton exchange membrane fuel cell I a hydrogen–air stack *J. Power Sources* **227** 72–9
[13] Abbas S C, Ding K, Liu Q, Huang Y, Bu Y, Wu J, Lv J, Ghausi M A and Wang Y 2016 Si–C–F decorated porous carbon materials: a new class of electrocatalysts for the oxygen reduction reaction *J. Mater. Chem.* A **4** 7924–9
[14] Cao R, Thapa R, Kim H, Xu X, Gyu Kim M, Li Q, Park N, Liu M and Cho J 2013 Promotion of oxygen reduction by a bio-inspired tethered iron phthalocyanine carbon nanotube-based catalyst *Nat. Commun.* **4** 2076
[15] Lin L, Zhu Q and Xu A W 2014 Noble-metal-free Fe−N/C catalyst for highly efficient oxygen reduction reaction under both alkaline and acidic conditions *J. Am. Chem. Soc.* **136** 11027–33
[16] Xie B, Zhang Y and Zhang R 2017 Coassembly and high ORR performance of monodisperse Pt nanocrystals with a mesopore-rich nitrogen-doped graphene aerogel *J. Mater. Chem.* A **5** 17544–8
[17] Duan J, Zheng Y, Chen S, Tang Y, Jaroniec M and Qiao S 2013 Mesoporous hybrid material composed of Mn_3O_4 nanoparticles on nitrogen-doped graphene for highly efficient oxygen reduction reaction *Chem. Commun.* **49** 7705–7
[18] Liang J, Zhou R F, Chen X M, Tang Y H and Qiao S Z 2014 Fe−N decorated hybrids of CNTs grown on hierarchically porous carbon for high-performance oxygen reduction *Adv. Mater.* **26** 6074–9
[19] Wang D and Astruc D 2017 The recent development of efficient earth-abundant transition-metal nanocatalysts *Chem. Soc. Rev.* **46** 816–54
[20] Du J, Cheng F, Wang S, Zhang T and Chen J 2014 M(salen)-derived nitrogen-doped M/C (M = Fe, Co, Ni) porous nanocomposites for electrocatalytic oxygen reduction *Sci. Rep.* **4** 4386
[21] Jiang K *et al* 2019 Highly selective oxygen reduction to hydrogen peroxide on transition metal single atom coordination *Nat. Commun.* **10** 3997

[22] Li K, Zhang R, Gao R, Shen G-Q, Pan L, Yao Y, Yu K, Zhang X and Zou J-J 2019 Metal-defected spinel $Mn_xCo_{3-x}O_4$ with octahedral Mn-enriched surface for highly efficient oxygen reduction reaction *Appl. Catal.* B **244** 536–45

[23] Zhang A, Wu J, Xue L, Yan S and Zeng S 2020 Probing heteroatomic dopant-activity synergy over Co_3O_4/doped carbon nanotube electrocatalysts for oxygen reduction reaction *Inorg. Chem.* **59** 403–14

[24] Zhang X, Lu P, Zhang C, Cui X, Xu Y, Qu H and Shi J 2017 Towards understanding ORR activity and electron-transfer pathway of M-N/C electro-catalyst in acidic media *J. Catal.* **356** 229–36

[25] Zhou L, Yang C, Wen J, Fu P, Zhang Y, Sun J, Wang H and Yuan Y 2017 Soft-template assisted synthesis of Fe/N-doped hollow carbon nanospheres as advanced electrocatalysts for the oxygen reduction reaction in microbial fuel cells *J. Mater. Chem.* A **5** 19343–50

[26] Han H, Noh Y, Kim Y, Jung W S, Park S and Kim W B 2019 An N-doped porous carbon network with a multidirectional structure as a highly efficient metal-free catalyst for the oxygen reduction reaction *Nanoscale* **11** 2423–33

[27] Zhang Z, Yang S, Li H, Zan Y, Li X, Zhu Y, Dou M and Wang F 2019 Sustainable carbonaceous materials derived from biomass as metal-free electrocatalysts *Adv. Mater.* **31** 1805718

[28] Gao L, Xiao M, Jin Z, Liu C, Zhu J, Ge J and Xing W 2018 Correlating Fe source with Fe−N−C active site construction: Guidance for rational design of high-performance ORR catalyst *J. Energy Chem.* **27** 1668–73

[29] Hou Y-N, Zhao Z, Zhang H, Zhao C, Liu X, Tang Y, Gao Z, Wang X and Qiu J 2019 Designed synthesis of cobalt nanoparticles embedded carbon nanocages as bifunctional electrocatalysts for oxygen evolution and reduction *Carbon* **144** 492–9

[30] Xu X, Zhang X, Xia Z, Sun R, Li H, Wang J, Yu S, Wang S and Sun G 2021 Solid phase microwave-assisted fabrication of Fe-doped ZIF-8 for single-atom Fe−N−C electrocatalysts on oxygen reduction *J. Energy Chem.* **54** 579–86

[31] Arul A, Pak H, Moon K U, Christy M, Oh M Y and Nahm K S 2018 Metallomacrocyclic-carbon complex: a study of bifunctional electrocatalytic activity for oxygen reduction and oxygen evolution reactions and their lithium−oxygen battery applications *Appl. Catal.* B **220** 488–96

[32] Li Q, Shao Q, Wu Q, Duan Q, Li Y and Wang H-g 2018 In situ anchoring of metal nanoparticles in the N-doped carbon framework derived from conjugated microporous polymers towards an efficient oxygen reduction reaction *Catal. Sci. Technol.* **8** 3572–9

[33] Jasinski R 1964 A new fuel cell cathode catalyst *Nature* **201** 1212–3

[34] Lu G, Zhu Y, Xu K, Jin Y, Ren Z J, Liu Z and Zhang W 2015 Metallated porphyrin based porous organic polymers as efficient electrocatalysts *Nanoscale* **7** 18271–7

[35] Ni B, Ouyang C, Xu X, Zhuang J and Wang X 2017 Modifying commercial carbon with trace amounts of ZIF to prepare derivatives with superior ORR activities *Adv. Mater.* **29** 1701354

[36] Ahn S H, Yu X and Manthiram A 2017 'Wiring' Fe−N_x -embedded porous carbon framework onto 1D nanotubes for efficient oxygen reduction reaction in alkaline and acidic media *Adv. Mater.* **29** 1606534

[37] Ye J-S, Wen Y, De Zhang W, Cui H-F, Ming Gan L, Qin Xu G and Sheu F-S 2004 Application of multi-walled carbon nanotubes functionalized with hemin for oxygen detection in neutral solution *J. Electroanal. Chem.* **562** 241–6

[38] Garino N *et al* 2019 Proving the existence of Mn porphyrin-like complexes hosted in reduced graphene oxide with outstanding performance as oxygen reduction reaction catalysts *2D Mater.* **6** 045001

[39] Sun C, Hu B, Zhao D and Liu Z 2013 Synthesis and structure of five or six-coordinate manganese deuteroporphyrin-niacin dyads with intramolecular axial pyridine *Dyes Pigments* **96** 130–7

[40] Eisenberg D, Stroek W, Geels N J, Sandu C S, Heller A, Yan N and Rothenberg G 2016 A simple synthesis of an N-doped carbon ORR catalyst: hierarchical Micro/Meso/Macro porosity and graphitic shells *Chem. Eur. J.* **22** 501–5

[41] Jia B and Gao L 2007 Fabrication of Fe_3O_4 core−shell polyhedron based on a mechanism analogue to Ostwald ripening process *J. Cryst. Growth* **303** 616–21

[42] Xu H, Wu X, Li X, Luo C, Liang F, Orignac E, Zhang J and Chu J 2018 Properties of graphene-metal contacts probed by Raman spectroscopy *Carbon* **127** 491–7

[43] Chen Y Z, Wang C, Wu Z Y, Xiong Y, Xu Q, Yu S H and Jiang H L 2015 From bimetallic metal-organic framework to porous carbon: high surface area and multicomponent active dopants for excellent electrocatalysis *Adv. Mater.* **27** 5010–6

[44] Zhu Q L, Xia W, Akita T, Zou R and Xu Q 2016 Metal-organic framework-derived honeycomb-like open porous nanostructures as precious-metal-free catalysts for highly efficient oxygen electroreduction *Adv. Mater.* **28** 6391–8

[45] Fan M, Pan X, Lin W and Zhang H 2020 Carbon-covered hollow nitrogen-doped carbon nanoparticles and nitrogen-doped carbon-covered hollow carbon nanoparticles for oxygen reduction *ACS Appl. Nano Mater.* **3** 3487–93

[46] Pan F, Zhang H, Liu K, Cullen D, More K, Wang M, Feng Z, Wang G, Wu G and Li Y 2018 Unveiling active sites of CO_2 reduction on nitrogen-coordinated and atomically dispersed iron and cobalt catalysts *ACS Catal.* **8** 3116–22

[47] Zhang J *et al* 2019 Tuning the coordination environment in single-atom catalysts to achieve highly efficient oxygen reduction reactions *J. Am. Chem. Soc.* **141** 20118–26

[48] Du Y, Liu L, Xiang Y and Zhang Q 2018 Enhanced electrochemical capacitance and oil-absorbability of N-doped graphene aerogel by using amino-functionalized silica as template and doping agent *J. Power Sources* **379** 240–8

[49] Feng S, Liu C, Chai Z, Li Q and Xu D 2018 Cobalt-based hydroxide nanoparticles@N-doping carbonic frameworks core−shell structures as highly efficient bifunctional electrocatalysts for oxygen evolution and oxygen reduction reactions *Nano Res.* **11** 1482–9

[50] Woo J, Yang S Y, Sa Y J, Choi W-Y, Lee M-H, Lee H-W, Shin T J, Kim T-Y and Joo S H 2018 Promoting oxygen reduction reaction activity of Fe–N/C electrocatalysts by silica-coating-mediated synthesis for anion-exchange membrane fuel cells *Chem. Mater.* **30** 6684–701

[51] Xing X, Liu R, Anjass M, Cao K, Kaiser U, Zhang G and Streb C 2020 Bimetallic manganese-vanadium functionalized N, S-doped carbon nanotubes as efficient oxygen evolution and oxygen reduction electrocatalysts *Appl. Catal.* B **277** 119195

[52] Zhao Y *et al* 2020 Cross-linked Polyphosphazene Hollow nanosphere derived N/P-doped porous carbon with single nonprecious metal atoms for oxygen reduction reaction *Angew. Chem., Int. Ed. Engl.* **132** 14747–54

[53] Mun Y, Lee S, Kim K, Kim S, Lee S, Han J W and Lee J 2019 Versatile strategy for tuning ORR activity of a single Fe−N_4 site by controlling electron-withdrawing/donating properties of a carbon plane *J. Am. Chem. Soc.* **141** 6254–6